Building an Iron Chromophore Incorporating Prussian Blue Analogue for Photoelectrochemical Water Oxidation

T. Gamze Ulusoy Ghobadi,[a] Amir Ghobadi,[b] Merve Demirtas,[a] Muhammed Buyuktemiz,[c] Kubra N. Ozvural,[d] Elif Akhuseyin Yildiz,[e] Emre Erdem,[f] H. Gul Yaglioglu,[e] Engin Durgun,[a] Yavuz Dede,[c] Ekmel Ozbay,*[a, b, g] and Ferdi Karadas*[a, d]

Abstract: The replacement of traditional ruthenium-based photosensitizers with low-cost and abundant iron analogs is a key step for the advancement of scalable and sustainable dye-sensitized water splitting cells. In this proof-of-concept study, a pyridinium ligand coordinated pentacyanoferrate(II) chromophore is used to construct a cyanide-based CoFe extended bulk framework, in which the iron photosensitizer units are connected to cobalt water oxidation catalytic sites through cyanide linkers. The iron-sensitized photoanode exhibits exceptional stability for at least 5 h at pH 7 and features its photosensitizing ability with an incident photon-to-current conversion capacity up to 500 nm with nano-second scale excited state lifetime. Ultrafast transient absorption and computational studies reveal that iron and cobalt sites mutually support each other for charge separation via short bridging cyanide groups and for injection to the semiconductor in our proof-of-concept photoelectrochemical device. The reorganization of the excited states due to the mixing of electronic states of metal-based orbitals subsequently tailor the electron transfer cascade during the photoelectrochemical process. This breakthrough in chromophore-catalyst assemblies will spark interest in dye-sensitization with robust bulk systems for photoconversion applications.

[a] T. G. U. Ghobadi, M. Demirtas, Prof. E. Durgun, Prof. E. Ozbay, Prof. F. Karadas
     UNAM – National Nanotechnology Research Center
     Institute of Materials Science and Nanotechnology
     Bilkent University
     06800 Ankara (Turkey)
     E-mail: ozbay@bilkent.edu.tr
            karadas@fen.bilkent.edu.tr

[b] A. Ghobadi, Prof. E. Ozbay
     Department of Electrical and Electronics Engineering and
     NANOTAM – Nanotechnology Research Center
     Bilkent University
     06800 Ankara (Turkey)

[c] M. Buyuktemiz, Prof. Y. Dede
     Department of Chemistry, Faculty of Science
     Gazi University
     Teknikokullar, 06500 Ankara (Turkey)

[d] K. N. Ozvural, Prof. F. Karadas
     Department of Chemistry, Faculty of Science
     Bilkent University, 06800 Ankara (Turkey)

[e] E. A. Yildiz, Prof. H. G. Yaglioglu
     Department of Engineering Physics, Faculty of Engineering
     Ankara University
     06100 Ankara (Turkey)

[f] Prof. E. Erdem
     Faculty of Engineering and Natural Sciences Sabanci University
     34956 Istanbul (Turkey)

[g] Prof. E. Ozbay
     Department of Physics, Faculty of Science
     Bilkent University
     06800 Ankara (Turkey)

     Supporting information for this article is available on the WWW under
     https://doi.org/10.1002/chem.202100654

Introduction

Earth-abundant photoactive complexes have become one of the central themes in light-harvesting applications, including dye-sensitized solar cells, artificial photosynthesis, photocatalysis, light-emitting diodes, and photodynamic therapy.[1] The main focus is centered on Fe(II) complexes owing to their earth-abundancy, low toxicity, and isovalency with the well-known precious, scarce, and expensive heavy metal (e.g. Ru(II), Os (II), Re(I), and Ir(III)) based photosensitizers.[2] The photoactivity of these complexes is governed by the metal-to-ligand charge transfer (MLCT) process, which is highly dependent on the electronic nature (donating & accepting ability) of the ligand and the interaction between the metal and the ligand. Since the relatively weak metal-ligand interactions in iron–bipyridyl complexes retard the MLCT process due to the readily accessible metal-centered (MC*) states, so-called deactivation pathways, positioned energetically below the MLCT states.[3] Common iron chromophores feature femtosecond range light-activated excited state lifetimes, which makes them unfeasible for solar to energy conversion devices. For example, the lifetime of MLCT excited state in the trisbipyridyl iron complex (below 100 fs) is much shorter than its ruthenium analog (approx. 100 ps).[4] The commonly employed strategy to enhance the lifetime of the MLCT state is to decorate the coordination sphere of the octahedral Fe(II) site with a combination of σ-donor and π-acceptor ligands. In this respect, the earlier studies revolve around the utilization of cyanoferrate(II) complexes including $Fe(bpy)_2(CN)_2$ and $[Fe(bpy)(CN)_4]^{2-}$.[5–7] Despite the presence of strongly σ-donating cyanide ligands, they still exhibit accessible low-lying MC* states relative to MLCT states.

Chemistry–A European Journal

Full Paper
doi.org/10.1002/chem.202100654

Chemistry Europe
European Chemical
Societies Publishing

Some encouraging developments have been achieved recently, particularly with iron complexes coordinated to strongly σ-donating cyclometalated ligands, which were found to effectively block deactivation pathways by destabilizing MC* states.[2] Recent MLCT lifetimes of 9 ps and 528 ps were achieved by Fe(II) carbene complexes surrounded with CNC and CC-type ligands, respectively.[8,9] A substantially longer excited-state lifetime of 37 ps was reported when an iron(II) carbene complex is immobilized on Al_2O_3.[10] The increasing number of potential iron chromophores gives the promise that *'iron can be the new ruthenium'*.[3,11] This breakthrough, however, is bound to a critical step, which is the incorporation of an iron chromophore into a dye-sensitized device and is awaiting realization.

Recently, numerous ruthenium-based photosensitizer-water oxidation catalyst assemblies have been highlighted in photoelectrochemical cells.[12–14] Ruthenium-based assemblies have been developed also within a cyanide framework.[15–17] Unfortunately, the implementation of an iron chromophore into an earth-abundant dye-sensitized (water oxidation) photoanode so far has not been nearly as successful as their heavy counterparts, since it presents a threefold problem: i) The MLCT excited-state lifetimes of iron complexes are not sufficient to drive interfacial charge transfer at the semiconductor surface, ii) they have relatively poor stabilities, and iii) the design of a bridging ligand that connects the iron chromophore to a catalyst, is a synthetic challenge. Along this line, a precious-metal free water oxidation catalyst (WOC) that is stable and that can be bridged to the iron chromophore is another major challenge that has not been explored yet.

Most of the WOCs, utilized for the dye-sensitized water oxidation process, are molecular ruthenium-based ones. So far, the replacement of molecular ruthenium with bulk oxides catalysts have only been possible with the expense of poor activity due to relatively high electron-hole recombination pathways.[18] Recently, we utilized a cyanide-based synthetic pathway to take advantage of the strengths of both the molecular and bulk approaches. The synthetic protocol is much simpler than that of molecular ruthenium ones due to the high reactivity of both atoms of the cyanide groups towards 3d transition metal ions. PS and WOC units could be connected through a pentacyanoiron unit in a one-step reaction, which affords a rigid extended framework. Note that, metal pentacyanometalates exhibit amorphous nature due to the bulky organic ligand coordinated to the $Fe(CN)_5$ group.[17,19] The organic ligand limits the dimensionality of the framework, thereby leads to the formation of a non-periodic bulk structure with random defect sites, which is desired for enhanced catalytic activity. In contrary to molecular chromophore-catalyst assemblies, the functional units form a rigid bulk structure, once they are connected. These assemblies could, thus, be described as non-periodic bulk structures, which consist of molecular photosensitizer and catalyst units. They were also observed to exhibit superior stability under photocatalytic and photoelectrochemical conditions due to relatively fast electron transfer between the components and the rigidity of the bulk structure.[20–22]

Herein, we move one step forward and transform the $Fe(CN)_5$ group from an electronic relay to a chromophore unit.

While a maximum of four cyanide ligands was coordinated to an iron site in previously studied cyanoiron chromophores,[5–7] in our design, five cyanide ligands are coordinated to the iron site to destabilize the MC* states further. Moreover, the remaining coordination sphere of the octahedral iron site is occupied by an electron-deficient cationic pyridinium group rather than a common bipyridyl ligand to facilitate the MLCT process.[23,24] The molecular donor-acceptor chromophore is then reacted with Co^{2+} ions to obtain an amorphous metal pentacyanometalate structure, which incorporates a photosensitizer coupled to a WOC unit through cyanide groups.

Results and Discussion

Photoanode assembly

The iron chromophore was obtained by mixing a transparent solution of 1-(4-pyridyl)pyridinium chloride (PP^+Cl^-) with a pale yellow solution of $Na_3[Fe(CN)_5NH_3]$, [Fe–NH_3], to afford $Na_2[Fe(CN)_5PP]$, [Fe–PP], with a dark red solution due to the MLCT process between the iron site and PP^+ group as described in the Supporting Information (Supplementary Note 1; Scheme S1 and Supplementary Video 1). It is then coated on the rutile TiO_2 nanowires (NWs) modified FTO electrode to obtain TiO_2/[Fe–PP], and reacted with Co^{2+} ions to obtain a CoFe–PP layer, [CoFe–PP], on the semiconductor (SC) surface, yielding TiO_2/[CoFe–PP] (Figure 1a,b). The proposed photoanode, thus, contains a cyanide-based extended framework coated over a semiconductor surface. Since both cyanide groups and pyridyl groups are known to interact with the TiO_2 surface, the Fe–PP group is believed to be randomly oriented on the TiO_2 surface to afford a non-periodic coordination network.[5,25] For the preparation of the target photoanode, an in situ synthetic procedure is adopted (see "Methods"), in which the iron chromophore-catalyst assembly is prepared on the semiconductor surface.[21,26] First, the TiO_2 electrode was sensitized with the iron chromophore, [Fe–PP], and then reacted with Co^{2+} ions to enforce a catalyst-chromophore-semiconductor order (Co–Fe–PP–TiO_2) and to improve the physical interaction between layers. The coating process on TiO_2 is repeated two times to extend the molecular structure to a bulk one via the coordination of dangling cyanide groups to Co^{2+} ions. The previous studies on Prussian blue (PB)-based photoelectrodes indicate that the number of repetitions in the coating process should be optimized carefully since the thickness of the PB layer plays a critical role in the stability and the activity of photoelectrode.[26,27] A thin layer below around 10 nm thickness of bulk structure should be optimized since a thin layer decomposes easily due to the lack of a rigid bulk structure while at thicknesses above 20 nm insulating nature of the PB layer results in a decrease in the photocurrent density.[21]

Infrared spectroscopy is utilized to enlighten the coordination modes in cyanide-based compounds, [Fe–NH_3], [Fe–PP], and [CoFe–PP]. Both reactions of the PP^+ group with [Fe–NH_3] and that of Co^{2+} ions with [Fe–PP] to obtain [Fe–PP] and [CoFe–PP], respectively, shift the cyanide stretch (ν_{CN}) slightly to

Chemistry–A European Journal

Full Paper
doi.org/10.1002/chem.202100654

Chemistry Europe
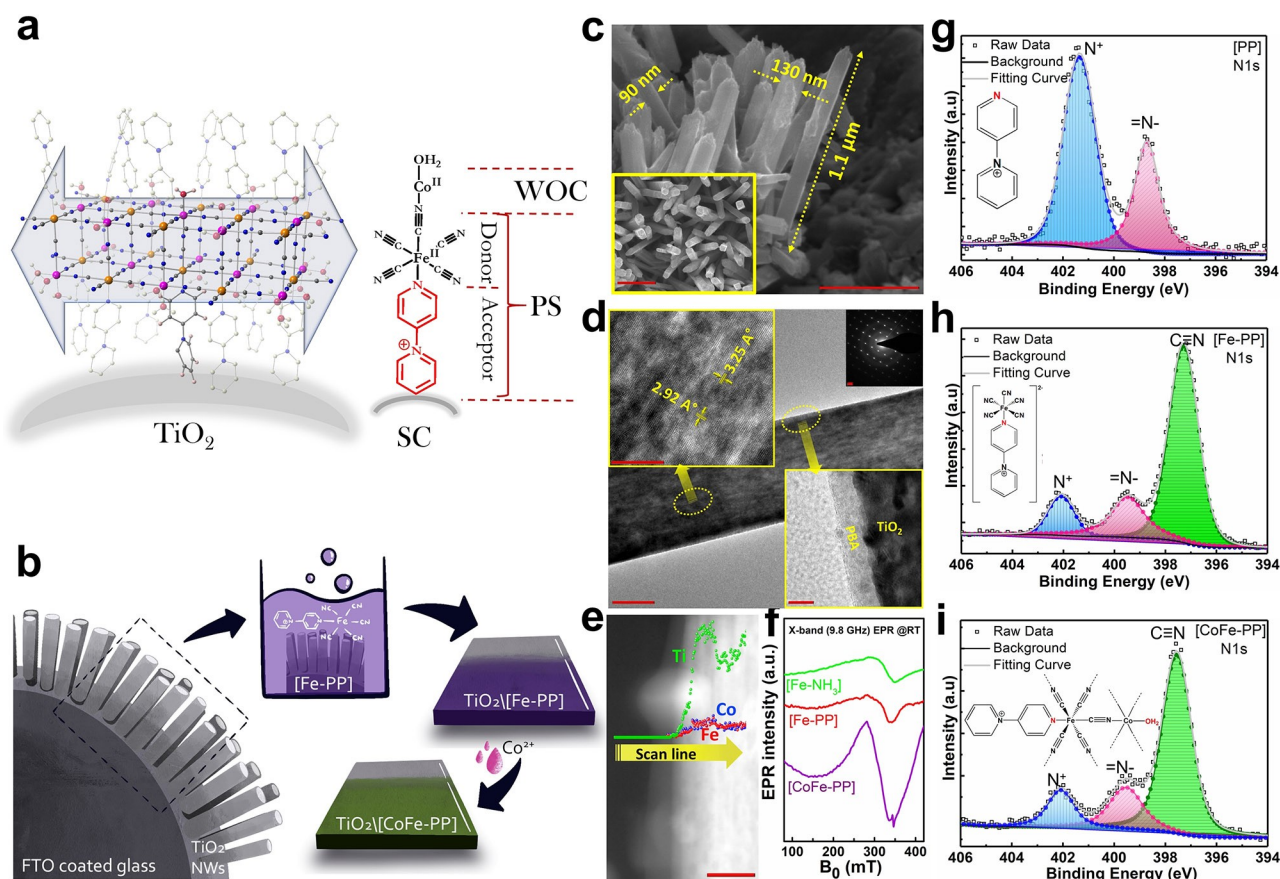European Chemical
Societies Publishing

Figure 1. Structural and morphological properties. (a) A rough illustration of an iron-sensitized photoanode and the role of each component displayed in the molecular fragment of the bulk [CoFe–PP] layer: TiO₂ is the semiconductor (SC), [Fe–PP] is the photosensitizer (PS), and cobalt site is the water oxidation catalyst (WOC). The grey arrow indicates the [CoFe–PP] extended framework on the TiO₂ surface. (b) Schematic illustration for the three-step preparation of TiO₂/[CoFe–PP] photoanode; (i) hydrothermal growth of TiO₂ NWs, (ii) coating TiO₂ NWs with [Fe–PP] to prepare TiO₂/[Fe–PP], and (iii) in situ drop-casting of Co²⁺ ions to prepare TiO₂/[CoFe–PP]. The color of the electrode changes from purple to green. (c) A side view SEM image of the TiO₂/[CoFe–PP] photoanode and the inset displays the top view of the NWs, scale bars: 500 nm. (d) HR-TEM of TiO₂/[CoFe–PP] shows its lattice fringes with interplanar spacings of 3.25 Å and 2.92 Å, which are consistent with the rutile phase. The down-right inset indicates the interface between the TiO₂ NW and a ~10 nm-thick PB layer, with a scale bar of 5 nm. The SAED pattern of a single NW, which is shown in the inset (top right), proves its single crystalline phase. (e) EDS line scan in HR-TEM from air to an individual PB coated TiO₂ NW with a high magnification of the interface, scale bar: 20 nm. (f) Room temperature X-band EPR spectra of [Fe–NH₃], [Fe–PP], and [CoFe–PP], revealing the nature of iron sites. (g–i) XPS N1s spectra of [PP], [Fe–PP], and [CoFe–PP].

higher wavenumbers (Supporting Information, Supplementary Note 2 and Figure S1a). The shift in [Fe–NH₃]→[Fe–PP] reactions is attributed to the electron-accepting behavior of [PP] group while the one in [Fe–PP]→[CoFe–PP] confirms the formation of a Fe–CN–Co coordination mode.[19] ν_{CN} for [CoFe–PP] is much broader than that for [Fe–PP] and also the ones for previously studied crystalline PBAs,[28,29] due to the formation of a non-periodic bulk structure. Top and cross-sectional scanning electron microscopy (SEM) images and high-resolution transmission electron microscopy (HR-TEM) analysis of the TiO₂/[CoFe–PP] photoanode confirms the formation of a non-periodic thin [CoFe–PP] layer with a thickness of around 10 nm, corresponding to roughly 5 Co–Fe–PP layers on the surface of TiO₂ NWs (with a 0.8–1.2 μm mean length and a ~70–140 nm diameter) (Figure 1c,d). The sharp selected area electron diffraction–(SAED) pattern and the RAMAN profile (Figure S1b) in the inset prove the growth of a single crystalline rutile phase of TiO₂ NWs. The energy dispersive X-Ray spectroscopy line

scan in TEM (TEM-EDS) is also performed in the vicinity of the NW surface to investigate the content of the elements on the NW surface (Figure 1e). The line scan confirms the presence of Fe and Co atoms on the surface of the photoanode. Furthermore, EPR spectroscopy was performed on powder samples to elucidate the nature of iron ions in the PS–WOC assembly. It is known that diamagnetic Fe²⁺ cannot be detected solely via EPR measurements. Nevertheless, a broad EPR signal at around g~2.2–2.3 could be observed for a high amount of magnetically interacting iron ions regardless of their oxidation states suggesting that the Fe–Fe (spin-spin) interactions dominate the EPR spectra.[30] The X-band EPR spectra measured at room temperature reveal a similar profile for [Fe–NH₃] and [Fe–PP] (Figure 1f). The broad line can be safely attributed to the dipolar interactions between low-spin Fe(III) sites with a coordination environment that reveals an EPR signal. On the other hand, [CoFe–PP] exhibits an additional distinct sharp signal at around g~2.00, which is assigned to magnetically

Chemistry–A European Journal

Full Paper
doi.org/10.1002/chem.202100654

**Chemistry
Europe**
European Chemical
Societies Publishing

isolated Fe^{3+} ions.[31,32] Therefore, the EPR results suggest that cobalt ions favor the $Fe^{II}-PP^+ \rightarrow Fe^{III}-PP$ MLCT process due to the donating ability of cobalt sites. The Gaussian signal broadening, compared to [Fe–NH$_3$] and [Fe–PP], is also enhanced due to the increase in the number of spin-spin exchange interactions (dipolar coupling) in the extended framework as expected. X-ray photoelectron spectroscopy (XPS) measurements performed on the [CoFe–PP] powder sample and the TiO$_2$/[CoFe–PP] electrode reveal three distinct peaks in N1s region (Figure 1g–i) and traditional peaks in Co2p and Fe2p regions, suggesting that a mixed-valent CoFe PB layer incorporating PP groups is formed (reasons detailed in Supplementary Note 3, and see Figures S2, S3, Tables S1, S2, Supporting Information).

Photoelectrochemical water oxidation

The characterization techniques presented herein reveal that our in situ synthetic method leads to the formation of a unique non-periodic bulk CoFe–PP layer on TiO$_2$ as desired. After the initial structural analysis, light induced photocurrent measurements in a three-electrode cell was conducted to elucidate the role of each component in a TiO$_2$/[CoFe–PP] photoanode at pH 7 under a 1 sun irradiation (Figure 2a and Figure S4). Since there are two photoactive materials, TiO$_2$ and [CoFe–PP], the transient current responses of the electrode under on-off cycles of illumination was monitored with different cut-off filters and compared to the bare TiO$_2$ electrode (Figure 2b and Figure S5a). While TiO$_2$ significantly contributes to the photocurrent density either in the absence of a filter and with the 420 nm-filter due to its absorption tail, the effect of iron chromophore becomes more dominant as longer wavelength cut-off filters are used.
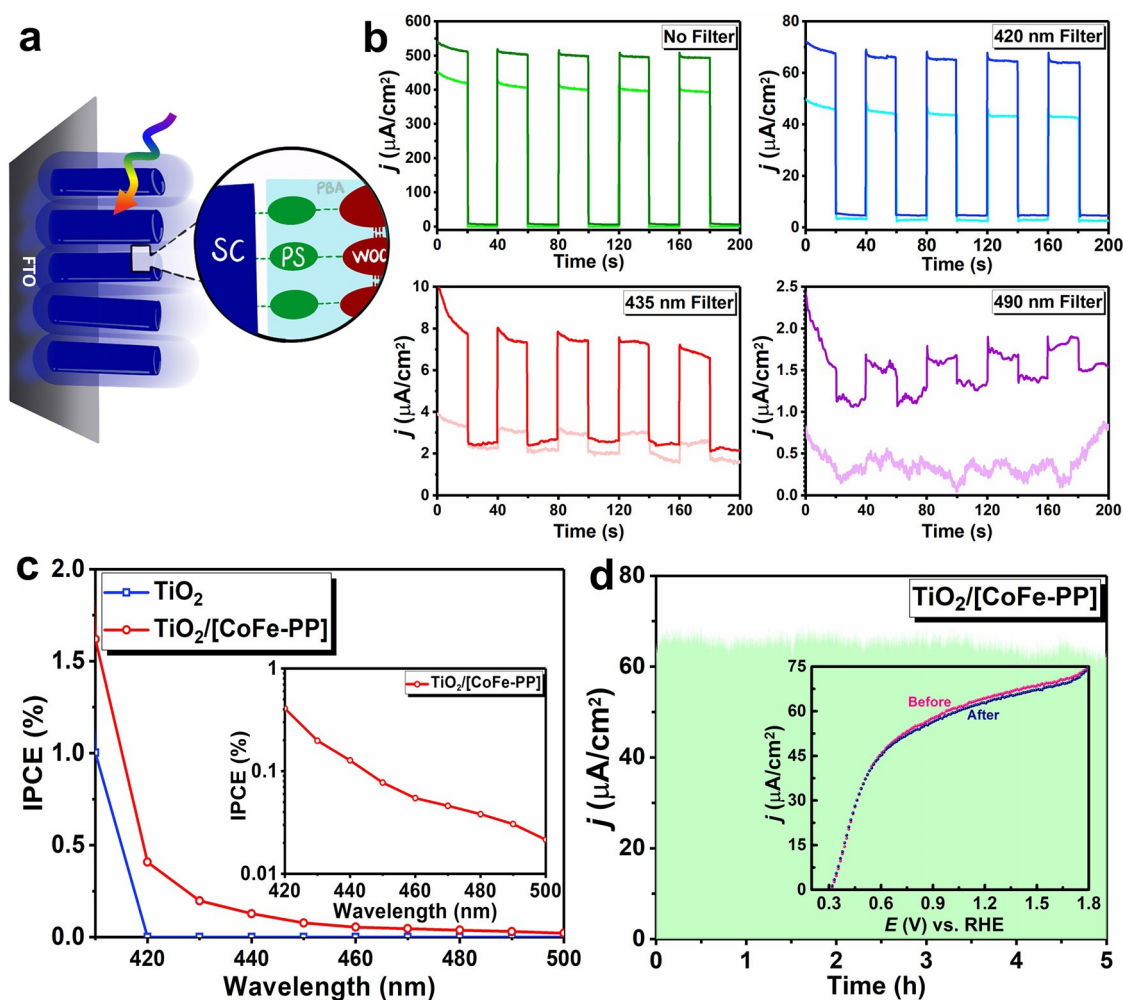

Figure 2. Photoelectrochemical studies. (a) Cross sectional illustration of TiO$_2$/[CoFe–PP] electrode model; (b) Pulsed chronoamperograms performed at 1.23 V$_{RHE}$ for 300 s for TiO$_2$/[CoFe–PP] electrodes (dark-colored lines) and the bare TiO$_2$ electrode (light-colored lines) under white-light illumination and with cut-off filters: 420, 435, and 490 nm, sequentially. Electrolyte: 0.1 M PBS pH 7, light intensity: 100 mWcm^{-2}. (c) IPCE spectra for TiO$_2$/[CoFe–PP] and bare TiO$_2$ NWs with a 1.23 V$_{RHE}$ external bias. The wavelength is scanned from 300 to 500 nm with a step of 10 nm. The inset shows a magnified image of IPCE in the 420–500 nm range. (d) Chronoamperogram of TiO$_2$/[CoFe–PP] for 5 h illumination at 1.23 V$_{RHE}$ bias with 420 nm filter. The inset shows LSV profiles, j-V measurement, before and after the long-term stability test.

Chemistry–A European Journal

Full Paper
doi.org/10.1002/chem.202100654

Chemistry Europe
European Chemical
Societies Publishing

TiO_2/[CoFe–PP] demonstrates a photo and dark current difference of approx. 5 $\mu A.cm^{-2}$ at 435 nm filtered case, while it is only 1 $\mu A.cm^{-2}$ for the bare one. For the 490 nm filtered case, TiO_2 is photo-irresponsive while TiO_2/[CoFe–PP] electrode is still active. In agreement with these findings, the incident photon-to-current conversion efficiency (IPCE) response for TiO_2/[CoFe–PP] is extended up to 500 nm with an exponential decline while the one for bare TiO_2 decays to zero just below 420 nm (Figure 2c). Note that, IPCE results confirm the photosensitizing ability of [Fe–PP] chromophore.

Besides the promising optical response of TiO_2/[CoFe–PP], the photoanode exhibits outstanding stability during a 5 h chronoamperometry (CA) experiment, at a bias voltage of 1.23 V_{RHE} (Figure 2d). To evaluate the stability of the photoelectrode, LSV is performed after CA and compared with the pristine profile, shown in Figure 2d inset, which shows almost the same photocurrent spectra. A similar experiment at 1.23 V_{RHE} (at pH 7), with 420 nm cut-off filter, was performed with a gas-tight cell and the amount of photogenerated O_2 was recorded by GC, yielding a Faradaic efficiency of approximately 80% (as explained in Figure S5b), indicating that the photocurrent response is mainly originating from the water oxidation process. Moreover, the photoanode exhibits a compatible water oxidation activity compared to previously reported PB based photoelectrodes (listed in Table S3). TEM-EDS and XPS analysis performed on the post-catalytic TiO_2/[CoFe–PP] electrode also confirms that TiO_2/[CoFe–PP] retains its morphology (Supporting Information, Supplementary Note 5; Figure S6, S7). TiO_2/[Fe–PP] electrode, however, degrades under the same conditions, which indicates the molecular Fe–PP complex decomposes under the same photoelectrochemical condition due to the loose coordination of monodentate PP group to the iron site. The evident enhancement in the stability of TiO_2/[CoFe–PP] compared to TiO_2/[Fe–PP], thus, demonstrates that the rigidity of the PB bulk structure plays a critical role in the long-term stability of the iron photosensitizer. (Supporting Information, Supplementary Note 6; Figure S8).

UV-Vis absorption profile

To gain an insight into the origin of the above promising results, the steady-state absorption measurements were conducted on both solutions and electrodes containing [Fe–PP] and [CoFe–PP] to understand the absorption behavior of the iron chromophore (Figure S9–S11). Further evidence on the effect of JG to the activity of the photoanode will be provided in the next sections. The molar extinction coefficient of [Fe–PP] is similar to those previously reported for potential iron chromophores.[33,34] The coordination of Co^{2+} ions shifts the MLCT band to shorter wavelengths (~430 nm) (Figure 3a). The weak band at ~615 nm is assigned to a metal-to-metal charge transfer (MMCT) transition (Fe^{III}–CN–Co^{II}→Fe^{II}–CN–Co^{III}) as it is depleted with the gradual addition of an oxidizing agent (1 M aqueous $Na_2S_2O_8$) to oxidize all of the metal ions to +3 oxidation states (Figure 3b).[35,36] The conservation of the MLCT band also confirms the stability of the iron chromophore under an oxidizing environment. Note that, the MLCT absorption band and IPCE profile for [CoFe–PP] perfectly match. To understand the absorption profiles of the molecular [Fe–PP] complex and non-periodic bulk [CoFe–PP] structure, different theoretical methods were employed.
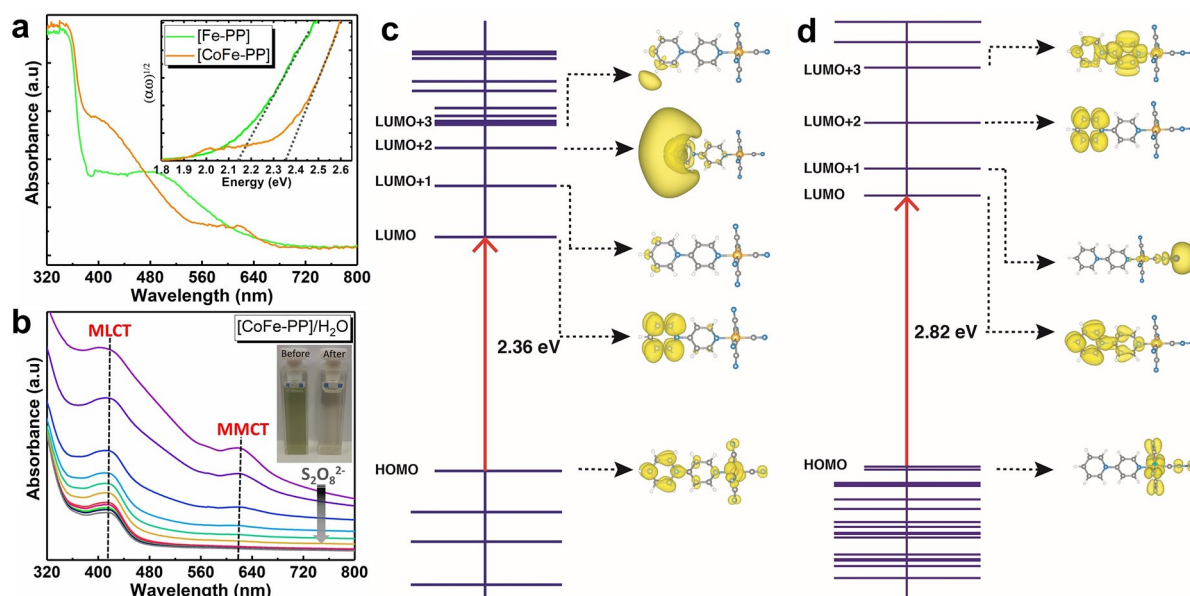

Figure 3. MLCT behavior of iron photosensitizer. (a) The absorption spectra for TiO_2/[Fe–PP] and TiO_2/[CoFe–PP] electrodes obtained by taking the bare TiO_2 electrode as reference. Inset shows the estimated optical band gaps of the same electrodes by extrapolating the line portion of the Tauc plot $(\alpha\omega)^{1/2}$ (α is the absorption coefficient and ω is the angular frequency) vs. hv. (b) Changes observed in the UV-Vis spectrum of an aqueous solution of the [CoFe–PP] complex with the incremental addition of 1 M aqueous $Na_2S_2O_8$ solution. Inset: Effectively depletion of the 2+ states visualized in the quartz cuvettes before and the final addition of $Na_2S_2O_8$. (c–d) The HOMO and LUMO levels with the electron clouds for [Fe–PP] and [CoFe–PP] are calculated with PBC-DFT using hybrid functionals in their lowest energy electronic states (S=0 for [Fe–PP] and S=3/2 for [CoFe–PP]).

Chemistry–A European Journal

Full Paper
doi.org/10.1002/chem.202100654

Chemistry Europe
European Chemical
Societies Publishing

First-principles electronic structure calculations based on density functional theory with periodic boundary conditions (PBC-DFT) and hybrid functionals (HSE06) were chosen first, since this level of calculations can be applied both for molecular and periodic bulk systems (i.e., electronic levels and electronic band structure) and yield correct magnetic and electronic ground state[37] (See theoretical calculations in the Supporting Information, Supplementary Note 8). The molecular configuration is reported as a prototype to better describe the MLCT mechanism and to enable comparisons with calculated excitation characteristics. In line with the experimental absorbance profile, PBC-DFT calculations performed on [PP], [Fe—PP], and [CoFe—PP] suggest that the HOMO-LUMO gap for [CoFe—PP] is larger compared to [Fe—PP] (Figure 3c,d and Figure S12). The nature of electronic states is also tuned with the coordination of Co^{2+} ions. The HOMO of [Fe—PP] is distributed over the Fe center as well as the PP ligand while that of [CoFe—PP] is fully localized on metal centers (both Co and Fe). Moreover, LUMO, LUMO+2, and LUMO+3 are dominantly located on the ligand center, which is an ideal molecular electronic level arrangement for an efficient MLCT process. The reported results are further confirmed with the atom-projected density of states (PDOS) analysis by calculating the relative contribution of orbitals projected on constituent atoms (Figure S13). Similar trends with narrowed HOMO-LUMO gap is obtained for bimolecular ([CoFe—PP]$_2$) configuration and with significantly reduced valance band maximum and conduction band minimum for an extended periodic system (Figure S14). The variation of the HOMO-LUMO gap (and/or electronic band gap) suggests that the structure of [CoFe—PP] fall within a molecular and an extended periodic configuration as expected. As correct magnetic state ordering can be obtained, the charge localization profile is not altered with the addition of on-site interaction energies (DFT+U) on transition metal centers (Figure S15).[37]

Excited state dynamics

Ultrafast transient absorption (TA) experiments were conducted to understand the charge transfer process at the femtosecond time scale. For both solution and photoanode designs, 400 nm pump excitation is utilized. The laser pulse energy is 1.5 μJ and to ensure the stability of the dyes, the absorption of the designs before and after experiment is measured. TA profiles of [Fe—PP] and [CoFe—PP] solutions provide clear evidence for the rapid population of the lowest excited state (Figure S16). The TA spectra of [Fe—PP] in EtOH show two main features; a broadband ground state bleaching (GSB) and a short-lived excited state absorption (ESA) signal, which indicate that the excited states are quenched into the lowest-lying state on the order of picoseconds. The short-lived ESA is, therefore, followed with a broadband GSB. However, the ultrafast carrier dynamics of the iron complex differs when it is coated on the semiconductor, TiO_2. Upon excitation with a 500 nm pump wavelength, the TA spectra of TiO_2/[Fe—PP] and TiO_2/[CoFe—PP] are recorded for a broad probe range (430–780 nm) (Figure 4a,b). The absorption difference in various pump-probe delay times indicates a

broadband ESA signal, which suggests that excited electrons are injected into TiO_2 CB with a high yield in an ultra-short time scale. The decay traces that are fitted into multiple exponential profiles reveal that TiO_2/[Fe—PP] shows dual lifetimes of 105.7 ps (11%) and 108.2 fs (89%) at 600 nm probe wavelength (Figure 4c). The lifetimes recorded for TiO_2/[CoFe—PP] are an order of magnitude longer with decay rates of 2.4 ns (3%), 7.8 ps (6%), and 71.7 fs (91%) (Figure 4d), which could be associated with the donating ability of cobalt ions due to the well-known metal-to-metal transfer (MMCT) ability between cobalt and iron sites in a CoFe PBA.[36] Cobalt sites, thus, serve as secondary donor groups to enhance MLCT ESA lifetime of the iron chromophore by feeding its ground state. The small portion (3%) of long-lived (2.4 ns) excited states also explains the relatively low photocurrent efficiency and weak IPCE.

Nevertheless, the nanosecond scale ESA lifetime for the iron chromophore is a record feature compared to previously reported iron photosensitizers, which assisting iron chromophore with a secondary metal ion can be a viable strategy to enhance the lifetime of MLCT state.

Electronic structural calculations and mechanism

The electronic structure calculations were further sought to investigate molecular orbitals. While PBC-DFT calculations were utilized to correlate HOMO-LUMO energy levels of both molecular and periodic model systems with experimental optical data and to investigate the origin of MLCT process, we herein performed quantum chemical calculations with DFT to elucidate the role of each component of the assembly on the charge transfer mechanism in the molecular level. Since the bulk structure could be considered as the non-periodic repetition of the bimetallic [CoFe—PP] molecular structure, organic PP, monometallic [Fe—PP], and bimetallic [CoFe—PP] molecular structures were studied in this section. This level of calculations has previously been employed by our team to investigate the water oxidation mechanism and charge transfer in PB-based systems.[20,21,28] The calculated molecular orbitals depicted in Figure 4e and Figure S17 reveal that [PP] and [Fe—PP] are radically different in their excitation characteristics. The local excitation motif calculated for bare [PP] no longer survives in the case of [Fe—PP] and a clear MLCT excitation is observed. The low spin Fe-center is involved in the excitation process. Calculated and measured spectra are in agreement with this view (Figure S18–S21, Table S4–S11). For [CoFe—PP], Co-d(z^2), d(x^2-y^2), and d(xz) orbitals energetically lie between Fe-centered HOMO and PP-centered LUMO, which is appropriate for an efficient hole transfer from the iron to cobalt site.

Consequently, the overall process is initiated with a Fe→PP MLCT process followed by a fast electron transfer from the LUMO of PP to the conduction band (CB) of TiO_2 (Note that the LUMO designation refers to the electronic structure before the electron transfer.). This MLCT process is followed by a hole transfer from the HOMO of Fe to a SOMO (singly occupied molecular orbital) on Co (MMCT). The proposed mechanism for the photoelectrochemical water oxidation mechanism in Fig-
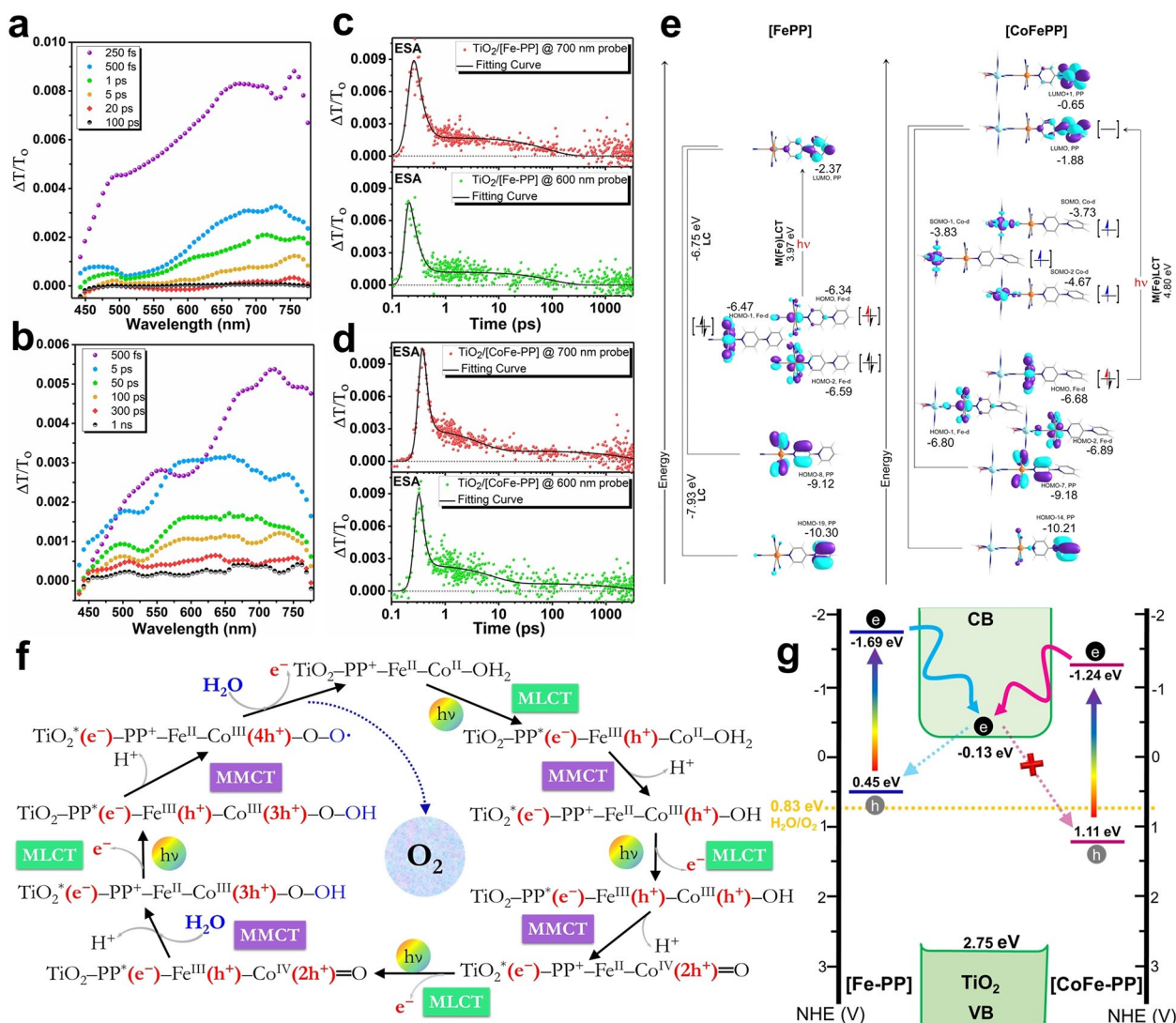
Chemistry–A European Journal

Full Paper
doi.org/10.1002/chem.202100654

Chemistry Europe
European Chemical
Societies Publishing

Figure 4. Mechanism and energy band alignment. (a–b) Femtosecond transient absorption dynamics of TiO₂/[Fe–PP] and TiO₂/[CoFe–PP] photoanodes at 500 nm (pump) excitation with different pump-probe time delays. (c–d) Decay dynamics for ESA signals TiO₂/[Fe–PP] and TiO₂/[CoFe–PP]. (e) Comparison of the excitation characteristics of [Fe–PP] and [CoFe–PP] in their lowest energy electronic states (S = 0 for the former and S = 3/2 for the latter. Converged Kohn-Sham orbitals are depicted. MO labels are included according to the location of the majority of the electron density. [Fe–PP] shows a clear MLCT transition. All SOMOs are localized on Co in [CoFe–PP]. (f) The proposed proton-coupled electron transfer (PCET) mechanism of the photoelectrochemical water oxidation for TiO₂/[CoFe–PP]: The 4e⁻ mechanism involves the oxidation and activation of the catalytic site by four PCET to yield a high-valent metal-oxo species.[28,38] This active species is attacked by a nucleophilic water molecule to form a peroxo species, which is then released as an oxygen molecule. (g) Schematic energy band diagram and carrier dynamics for TiO₂/[Fe–PP] and TiO₂/[CoFe–PP] showing the band alignments between different interfaces and the involved water oxidation electron transfer process.

ure 4f indicates that MMCT and MLCT transitions play active roles in the charge separation process. The electronic structure calculations, as well as experimental studies, suggest the presence of partial localization of distinct valences in [CoFe–PP], which is utilized for enhancing the ESA lifetime of the iron chromophore and, therefore, the charge separation process during the water oxidation process. The MMCT process is efficient thanks to the short bridging cyanide group promoting the cobalt sites to both a donor group that enhances the ESA lifetimes of the iron chromophore and a WOC that is activated once the holes are received from iron sites. We have reported a similar role for cobalt sites in previous works where Co is

participating in the catalytic cycle after the electron transfer to TiO₂ takes place.[21] In this work, we show that cobalt sites can also be utilized to build an iron-sensitized water oxidation photoanode. Furthermore, the band alignment of the heterostructure, which is constructed with a combination of optical and photoelectrochemical measurements (Supporting Information, Supplementary Note 11; Figures S22–S24; Table S12), clearly shows the effect of electron-donating cobalt sites to the energy levels of [Fe–PP]. The improper large energy difference between LUMO of [Fe–PP] and the CB of TiO₂, see Figure 4g, which can lead to back-reaction and carrier's recombination,[10,39] is renovated with the coordination of Co

Chemistry–A European Journal

Full Paper
doi.org/10.1002/chem.202100654

Chemistry Europe
European Chemical
Societies Publishing

ions to [Fe—PP]. In [CoFe—PP], proper alignment is achieved between the valence band (VB) of TiO$_2$, the HOMO level of [CoFe—PP], and the water oxidation energy level. A larger energetic barrier is also created between TiO$_2$ CB and the HOMO of [CoFe—PP], which hampers the recombination pathways. Moreover, a more favorable band level promotes the participation of more photogenerated holes in the water oxidation process. Catalytic cobalt sites, therefore, transform the energetic levels of the iron chromophore in the desired fashion for enhanced charge separation and water oxidation activity.

Conclusion

In this work, we show that a donor-acceptor iron photo-sensitizer can be achieved by slightly tuning the regular Prussian blue synthesis by utilizing a pyridinium ligand coordinated pentacyanoferrate complex as the starting precursor. The straightforward synthetic methodology also allows for the formation of a non-periodic bulk structure, which exhibits an efficient MLCT and MMCT process on the iron site. The working principle and the performance of the photoanode were elucidated with computational models (DFT, PBC-DFT, and TD-DFT), transient absorption, spectroscopic, and photoelectrochemical measurements. The MMCT process – a critical process in the water oxidation mechanism – reveals the active role of cobalt sites as donating groups in addition to their role as the WOC unit. Cyanide ligand, on the other hand, serves as i) a short bridging group to facilitate the MMCT process, ii) a strong field ligand to deactivate the undesired MC* states, and iii) a strong electron-donating group to increase the donor ability of iron site toward the acceptor pyridinium group. Moreover, an electron-deficient cationic pyridinium ligand is preferred over the commonly employed bipyridyl groups to enhance the MLCT process.

Photoelectrochemical studies disclose the remarkable stability of the photoelectrode even during a 5 h chronoamperometry study. Moreover, iron chromophore extends the absorption capacity of the bare electrode up to approx. 500 nm, which is in good accordance with the absorption profile of [CoFe—PP]. ESA lifetime is prolonged from approx. 200 ps for TiO$_2$/[Fe—PP] to above 1 ns for TiO$_2$/[CoFe—PP], mainly due to the donating ability of cobalt sites toward iron centers, which is also described based on quantum chemical calculations.

This proof-of-concept study marks the first demonstration of an iron-sensitized water oxidation photoanode. Since the simple synthetic pathway allows for the easy tuning of components of the photoanode, including the semiconductor and the acceptor group, further studies will be conducted to expand the portfolio of iron sensitized water oxidation photoanodes for a better understanding of this new generation of dye-sensitized photoelectrodes.

Experimental Section

Materials and methods

All of the chemicals were used as received without further purification. 1-(4-pyridyl) pyridinium chloride hydrochloride (C$_{10}$H$_9$ClN$_2$·HCl) denoted as [PP], sodium nitroferricyanide or sodium nitroprusside (Na$_2$[Fe(CN)$_5$NO]·2H$_2$O), sodium hydroxide (NaOH), ammonium hydroxide solution (NH$_4$OH, 25% (v/v)), ethanol (EtOH), methanol (MeOH), and cobalt(II) nitrate hexahydrate (Co-(NO$_3$)$_2$·6H$_2$O) were all purchased from Sigma-Aldrich. Titanium (IV) butoxide (Ti(OBu)4, 97%, Sigma-Aldrich), hydrochloric acid (HCl, 36%, Sigma-Aldrich), and Millipore deionized water (resistivity: 18 MΩ cm^{-1}) was used for the hydrothermal growth of TiO$_2$ nanowires on FTO coated glass (2 mm thick, 7 Ω sq^{-1}, Solaronix). Potassium phosphate buffer solutions were prepared by 0.1 M KH$_2$PO$_4$ and 0.1 M K$_2$HPO$_4$. Deionized water was used in all of the experiments.

Synthesis of pentacyanoferrate-coordinated 1-(4-pyridyl) pyridinium chloride hydrochloride, Na$_2$Fe(CN)$_5$(C$_{10}$H$_9$N$_2$) xH$_2$O, [Fe—PP]: Sodium aminopentacyanoferrate, Na$_3$[Fe(CN)$_5$NH$_3$]·3H$_2$O denoted as [Fe—NH$_3$] was synthesized according to our previously reported procedures.[19,20] For the synthesis of the iron chromophore, [Fe—PP], [PP] (1.23 mmol) was dissolved in ~1 mL of distilled water at room temperature. At that point, a colorless solution was observed. 1.23 mmol of [Fe—NH$_3$] was added into that solution with the addition of 1 mL more distilled water again and the color changed suddenly from transparent to dark red. The reaction was allowed to continue mixing in a covered flask for 6 hours in the dark at room temperature. Since the solubility of the compound in ethanol is less than those of the precursors, 30 mL cold EtOH was added to the solution and stored at 4°C in a refrigerator overnight. The unreacted [Fe(CN)$_5$NH$_3$]$^{3-}$ complex and possible by-products were removed by filtration and washed with 50 mL cold ethanol. The dark purple precipitate was isolated and dried under vacuum overnight at room temperature. The yield was around 65%.

Synthesis of cobalt pentacyanoferrate-coordinated 1-(4-Pyridyl) pyridinium, CoFe(CN)$_5$(C$_{10}$H$_9$N$_2$)·xH$_2$O, [CoFe—PP]: First, 1 equiv. Co(NO$_3$)$_2$ in distilled water was added dropwise into an aqueous solution of [Fe—PP] compound (113.75 mg, 23 mmol). To collect the solid and remove soluble unreacted species, the suspension was centrifuged three times at 6,500 rpm for 20 min. with water. The obtained olive green colored product was dried in an oven at 65°C for a day, see Scheme S1 (Supporting Information) for the chemical structure.

Synthesis of photoanodes: Pristine TiO$_2$ NWs "TiO$_2$", and in situ Prussian blue modified dye-sensitized TiO$_2$ electrode (Co WOC and iron chromophore loaded TiO$_2$ NWs) "TiO$_2$/[CoFe—PP]" were coated on FTO electrodes with an exposed area of 2 cm^2. TiO$_2$ NW arrays were synthesized by modifying the hydrothermal technique as described in our previous study.[40] For the preparation of TiO$_2$/[CoFe—PP] photoanode, bare NWs are first immersed into an EtOH solution containing [Fe—PP] (1.33 mM) for about a day at room temperature. Afterward, weakly absorbed dye molecules are removed by rinsing with copious amount of ethanol and the electrode is dried for 15 min. Then, 400–500 μL of 0.04 M Co(NO$_3$)$_3$ in EtOH solution is drop-casted on the electrode surface. The sample is washed after 15 min to remove unreacted Co^{2+} ions. This procedure is repeated 2–3 times to ensure a uniform Prussian blue layer on TiO$_2$. Finally, the TiO$_2$/[CoFe—PP] electrode is left for drying at room temperature.

General characterization instruments: X-band (9.86 GHz) EPR measurements were performed with Bruker EMXNano spectrometer. The magnetic field was determined using an NMR gaussmeter

(ER 035 M, Bruker); for magnetic-field calibration, polycrystalline DPPH with g = 2.0036 was used, which is already integrated into the spectrometer. IR spectra were measured using a Bruker ALPHA Platinum-ATR spectrometer in the wavenumber range 4000–400 cm^{-1}. X-ray photoelectron spectroscopy (XPS, Thermo Fisher Scientific, Al K-Alpha radiation, hυ = 1486.6 eV) measurement was also performed at survey mode by operating a flood gun for surface charge neutralization with 30 eV pass energy, 0.1 eV step size, and it was performed for determining the elemental analysis. Since charge compensation may not be sufficient in eliminating all surface charge, the peak positions correction was calibrated by referencing the C1s peak position (284.8 eV) and shifting other peaks in the spectrum accordingly. Raman spectroscopy measurements were performed with WITecAlpha 300S scanning near-field optical microscope with Raman module. The inset of Figure 1d shows the RAMAN spectrum of pristine TiO_2 NW arrays conforming its rutile phase with the fingerprinting at 143, 238, 443, 612, and 824 cm^{-1}, the observation of which is consistent with a former study.[41] Scanning electron microscopy (SEM, FEI – Quanta 200 FEG) was used to characterize the morphology, and elemental composition using an energy dispersive X-ray detector (EDX) coupled to the SEM operated at 15 kV. A transmission electron microscope (TEM, Tecnai G2-F30, FEI) was operated at 200 kV. TEM samples were dispersed in ethanol and prepared on a holey carbon-coated copper grid.

Photoelectrochemical measurements: Gamry Instruments (Interface 1000 Potentiostat/Galvanostat) was used for three-electrode photoelectrochemical experiments (as shown in Figure S4, Supporting Information). In this setup, the counter electrode is Pt mesh, and Ag|AgCl|KCl$_{(sat.)}$ is the reference electrode. A 0.1 M phosphate-buffered saline (0.5 M Na_2SO_4 in 0.1 M PBS, pH 7) is used as an electrolyte. Prior to each experiment, the electrolyte was purged with N_2 gas (with 99.999% purity) for about half an hour to remove O_2 from the cell. As the optical light source, the solar light simulator (Sciencetech, Model SLB-300B, 300 W Xe lamp, AM 1.5 global filter) with 100 mW/cm^2 output power density was used. The LSV and CV measurements were performed with a 50 mV/s scanning rate. To have a better qualitative comparison, all measured potentials in Ag/AgCl scale was converted into RHE standard.

Incident photon-to-current conversion efficiency (IPCE) was utilized to find the spectral response of the samples. In an IPCE setup, a Xe lamp is used as the light source, and its output was entered into a monochromator and then focused on the photoelectrode in a 3-electrode system. The generated current under light illumination was measured in our desired voltage bias (1.23 V$_{RHE}$) throughout a wavelength range spanning from 400 nm to 500 nm, with a step of 10 nm. Afterward, same experiment is performed on the samples under dark condition. The difference between these two currents was used as the photocurrent in the specific wavelength value. Finally, IPCE is calculated by following Equation (1):

$$IPCE\ (\%) = (1240/\lambda) \times \left(j/P_{light}\right) \times 100 \qquad (1)$$

where j, λ, and P_{light} represent the photocurrent density (mA cm^{-2}), wavelength (nm), and the output power density of the monochromatic light (mW cm^{-2}) at every wavelength value.

Theoretical calculations: Two types of electronic structure calculations were employed. Previously we have deduced our conclusions on calculations of small fragments of the catalyst, i.e. molecular models were used. We have successfully explained the experimentally observed phenomena with those molecular calculations.[20,28,42]

Herein we again kept our single molecule approach, however, strengthened it with calculations on the extended network where we have employed PBC. The primary goal of the first principles PBC calculations is to work with a more complete/correct description of the catalyst assembly and to predict the HOMO-LUMO bandgap. Note that the exact atomistic details of the extended catalyst network cannot be completely known and we are also reporting ab initio calculations of a bulk phase. It is nice to see that the experimentally obtained energies fall in between a molecular and a calculated perfect crystalline structure. This might indicate that the real system possesses a substantial amount of disordered sites as well and hence is a non-periodic extended structure.

The molecular system is also required since we can study the excitations (TD-DFT calculations) only with the molecular approach. Therefore, calculations on the network provide the electronic character of the states and energies that are comparable to the experimental values. Molecular calculations provide qualitative data on energies and excitations. Note that calculations on the extended system and molecular calculations agree in their deductions. The only difference is in the magnitude of the energies and since the molecular system uses a small, truncated model we do not dwell on the energies calculated with the molecular model. On the other hand, despite the small size of the molecular model, we have successfully employed it in drawing qualitative conclusions on the electronic structure of the ground states and characters of excitations.

The first-principles electronic structure calculations based on density functional theory with periodic boundary conditions (PBC-DFT) were employed by using Vienna Ab initio Simulation Package (VASP).[43–46] The generalized gradient approximation (GGA-PBE) was chosen to describe the exchange-correlation functional.[47] The projected augmented wave (PAW) method[48] with a kinetic energy cutoff of 520 eV was used to define element potentials. All of the molecules were isolated in a cubic cell with a vacuum space of 15 Å to prevent a spurious interaction between periodic images. The structural relaxations were performed by using conjugate gradient optimization allowing 10^{-5} eV energy tolerance between two sequential steps and allowing a maximum of 0.01 eV/Å force on atoms. On top GGA-PBE, Heyd-Scuseria-Ernzerhof (HSE06) hybrid functional approach, which is formed by mixing 25% of the Fock exchange with 75% of the PBE exchange and 100% of the PBE correlation energy was employed to elucidate molecular levels more accurately.[49] To treat the strong on-site Coulomb interaction of localized d-electrons, DFT+U method was also applied by using Dudarev approach, and apart from HOMO-LUMO gaps, similar electron localization features were obtained.[37]

Quantum chemical calculations were performed using the Density Functional Theory (DFT)[50–53] as implemented in the Gaussian 09 software suit.[54] Molecular fragments were employed in the chemical model. Geometries were fully optimized with B3LYP[52,55] functional and effective core potential of Hay and Wadt, LANL2DZ,[56,57] without any constraints on the symmetry. Vibrational frequency calculations on the optimized geometries ensured that the geometries correspond to the minima. Dunning's correlation consistent triple zeta basis set, cc-pVTZ,[58] was used in single point runs. This level of theory was found to be adequate for the description of electronic states and their relative energies in recent works.[20,21,28] All possible spin states were evaluated to identify the ground electronic states for all structures. Discussions were based on the ground electronic states, i.e. S = 0 for PP and [Fe–PP], and S = 3/2 for [CoFe–PP].

Time Dependent Density Functional Theory (TD-DFT) was employed for calculating electronic absorption spectra in combination with the triple zeta, cc-pVTZ[58] basis set. Long range corrected functional of Yanai,[59] CAM–B3LYP, is used for the TD-DFT calculations. CAM–B3LYP was found to be successful for the correct evaluation

of excitation behavior in similar systems.[20,21] Solvent environment is modeled with the PCM approach[60–62] utilizing the parameters of ethanol and water as implemented in Gaussian 09. Excitations with small oscillator strengths ($f < 0.02$) were excluded from the discussions. Molecular orbitals were plotted with the Chemcraft Program[63] using a contour value of 0.03.

Transient absorption studies: For TA measurements, a Ti: Sapphire laser optical parametric amplifier (Spectra Physics, Spitfire Pro XP, TOPAS) was utilized. The pulse duration and repetition rate of the laser beam was 52 fs and 1 KHz, respectively. Pump-probe setup (Spectra Physics, Helios) was integrated with a white light continuum probe source. To ensure the output laser characteristics, pulse duration measurement was performed by cross-correlation within the pump-probe system and the output was found to be 120 fs. The pump wavelength was selected based on the steady-state absorption spectra of the samples. Finally, to analyse the measured TA data, surface Xplorer software was employed.

Conflict of Interest

The authors declare no conflict of interest.

[1] O. S. Wenger, *J. Am. Chem. Soc.* **2018**, *140*, 13522–13533.
[2] Y. Liu, P. Persson, V. Sundström, K. Wärnmark, *Acc. Chem. Res.* **2016**, *49*, 1477–1485.
[3] O. S. Wenger, *Chem. A Eur. J.* **2019**, *25*, 6043–6052.
[4] J. K. McCusker, *Science* **2019**, *363*, 484–488.
[5] M. Yang, D. W. Thompson, G. J. Meyer, *Inorg. Chem.* **2002**, *41*, 1254–1262.
[6] M. Yang, D. W. Thompson, G. J. Meyer, *Inorg. Chem.* **2000**, *39*, 3738–3739.
[7] D. C. Ashley, E. Jakubikova, *Coord. Chem. Rev.* **2017**, *337*, 97–111.
[8] Y. Liu, T. C. B. Harlang, S. E. Canton, P. Chábera, K. Suárez-Alcántara, A. Fleckhaus, D. A. Vithanage, E. Göransson, A. Corani, R. Lomoth, V. Sundström, K. Wärnmark, *Chem. Commun.* **2013**, *49*, 6412–6414.
[9] P. Chábera, K. S. Kjaer, O. Prakash, A. Honarfar, Y. Liu, L. A. Fredin, T. C. B. Harlang, S. Lidin, J. Uhlig, V. Sundström, R. Lomoth, P. Persson, K. Wärnmark, *J. Phys. Chem. Lett.* **2018**, *9*, 459–463.
[10] T. C. B. Harlang, Y. Liu, O. Gordivska, L. A. Fredin, C. S. Ponseca, P. Huang, P. Chábera, K. S. Kjaer, H. Mateos, J. Uhlig, R. Lomoth, R. Wallenberg, S. Styring, P. Persson, V. Sundström, K. Wärnmark, *Nat. Chem.* **2015**, *7*, 883–889.
[11] J. D. Braun, I. B. Lozada, C. Kolodziej, C. Burda, K. M. E. Newman, J. van Lierop, R. L. Davis, D. E. Herbert, *Nat. Chem.* **2019**, *11*, 1144–1150.
[12] Z. Yu, F. Li, L. Sun, *Energy Environ. Sci.* **2015**, *8*, 760–775.
[13] M. K. Brennaman, R. J. Dillon, L. Alibabaei, M. K. Gish, C. J. Dares, D. L. Ashford, R. L. House, G. J. Meyer, J. M. Papanikolas, T. J. Meyer, *J. Am. Chem. Soc.* **2016**, *138*, 13085–13102.
[14] P. Xu, N. S. McCool, T. E. Mallouk, *Nano Today* **2017**, *14*, 42–58.
[15] Y. Aratani, K. Oyama, T. Suenobu, Y. Yamada, S. Fukuzumi, *Inorg. Chem.* **2016**, *55*, 5780–5786.
[16] Y. Aratani, T. Suenobu, K. Ohkubo, Y. Yamada, S. Fukuzumi, *Chem. Commun.* **2017**, *53*, 3473–3476.
[17] Z. Kap, F. Karadas, *Faraday Discuss.* **2019**, *215*, 111–122.
[18] J. T. Kirner, R. G. Finke, *ACS Appl. Mater. Interfaces* **2017**, *9*, 27625–27637.
[19] M. Aksoy, S. V. K. Nune, F. Karadas, *Inorg. Chem.* **2016**, *55*, 4301–4307.
[20] T. G. U. Ghobadi, E. A. Yildiz, M. Buyuktemiz, S. Sadigh Akbari, D. Topkaya, Ü. İsci, Y. Dede, H. G. Yaglioglu, F. Karadas, *Angew. Chem. Int. Ed.* **2018**, *57*, 17173–17177; *Angew. Chem.* **2018**, *130*, 17419–17423.
[21] T. G. U. Ghobadi, A. Ghobadi, M. Buyuktemiz, E. A. Yildiz, D. B. Yildiz, H. G. Yaglioglu, Y. Dede, E. Ozbay, F. Karadas, *Angew. Chem. Int. Ed.* **2020**, *59*, 4082–4090; *Angew. Chem.* **2020**, *132*, 4111–4119.
[22] T. G. U. Ghobadi, A. Ghobadi, M. Demirtas, R. Phul, E. A. Yildiz, H. G. Yaglioglu, E. Durgun, E. Ozbay, F. Karadas, *Cell Rep. Phys. Sci.* **2021**, *2*, 100319.
[23] B. J. Coe, J. L. Harries, M. Helliwell, L. A. Jones, I. Asselberghs, K. Clays, B. S. Brunschwig, J. A. Harris, J. Garin, J. Orduna, M. Halliwell, L. A. Jones, I. Asselberghs, K. Clays, B. S. Brunschwig, J. A. Harris, J. Garin, J. Orduna, *J. Am. Chem. Soc.* **2006**, *128*, 12192–12204.
[24] I. Deligkiozi, E. Voyiatzis, A. Tsolomitis, R. Papadakis, *Dyes Pigm.* **2015**, *113*, 709–712.
[25] M. Yang, D. W. Thompson, G. J. Meyer, *Inorg. Chem.* **2000**, *39*, 3738–3739.
[26] T. G. U. Ghobadi, A. Ghobadi, M. C. Soydan, M. B. Vishlaghi, S. Kaya, F. Karadas, E. Ozbay, *ChemSusChem* **2020**, *13*, 2577–2588.
[27] F. S. Hegner, I. Herraiz-Cardona, D. Cardenas-Morcoso, N. López, J. R. Galán-Mascarós, S. Gimenez, *ACS Appl. Mater. Interfaces* **2017**, *9*, 37671–37681.
[28] E. P. Alsaç, E. Ülker, S. V. K. Nune, Y. Dede, F. Karadas, *Chem. A Eur. J.* **2018**, *24*, 4856–4863.
[29] S. Goberna-Ferrón, W. Y. Hernández, B. Rodríguez-García, J. R. Galán-Mascarós, *ACS Catal.* **2014**, *4*, 1637–1641.
[30] A. Bhattacharyya, M. P. Schmidt, E. Stavitski, C. E. Martínez, *Org. Geochem.* **2018**, *115*, 124–137.
[31] B. M. Weckhuysen, R. Heidler, R. A. Schoonheydt, *Mol. Sieves* **2004**, *4*, 295–335.
[32] Y. Zhao, X. Jia, G. Chen, L. Shang, G. I. N. Waterhouse, L. Z. Wu, C. H. Tung, D. Ohare, T. Zhang, *J. Am. Chem. Soc.* **2016**, *138*, 6517–6524.
[33] P. Chábera, Y. Liu, O. Prakash, E. Thyrhaug, A. El Nahhas, A. Honarfar, S. Essén, L. A. Fredin, T. C. B. Harlang, K. S. Kjær, K. Handrup, F. Ericson, H. Tatsuno, K. Morgan, J. Schnadt, L. Häggström, T. Ericsson, A. Sobkowiak, S. Lidin, P. Huang, S. Styring, J. Uhlig, J. Bendix, R. Lomoth, V. Sundström, P. Persson, K. Wärnmark, *Nature* **2017**, *543*, 695–699.
[34] M. Glöckle, W. Kaim, *Angew. Chem. Int. Ed.* **1999**, *38*, 3072–3074; *Angew. Chem.* **1999**, *111*, 3262–3264.
[35] S. I. Ohkoshi, H. Tokoro, *Acc. Chem. Res.* **2012**, *45*, 1749–1758.
[36] D. Aguilà, Y. Prado, E. S. Koumousi, C. Mathonière, R. Clérac, *Chem. Soc. Rev.* **2016**, *45*, 203–224.
[37] F. S. Hegner, J. R. Galán-Mascarós, N. López, *Inorg. Chem.* **2016**, *55*, 12851–12862.
[38] B. M. Pires, P. L. Dos Santos, V. Katic, S. Strohauer, R. Landers, A. L. B. L. B. Formiga, J. A. Bonacin, P. L. Dos Santos, V. Katic, S. Strohauer, R. Landers, A. L. B. L. B. Formiga, J. A. Bonacin, *Dalton Trans.* **2019**, *48*, 4811–4822.
[39] K. S. Kjær, S. Styring, P. Persson, A. Honarfar, J. Uhlig, T. Ericsson, J. Bendix, K.-E. Bergquist, K. Wärnmark, O. Prakash, A. Yartsev, N. W. Rosemann, O. Gordivska, P. Chábera, D. Strand, L. Lindh, N. Kaul, R. Lomoth, L. A. Fredin, L. Häggström, P. Huang, V. Sundström, *Science* **2018**, *253*, 249–253.
[40] A. Ghobadi, T. G. U. Ghobadi, F. Karadas, E. Ozbay, *Sci. Rep.* **2018**, *8*, 1–12.
[41] T. G. U. Ghobadi, A. Ghobadi, A. K. Okyay, *J. Mater. Chem. A* **2014**, *2*, 16867–16876.
[42] E. A. Turhan, S. V. K. Nune, E. Ülker, U. Şahin, Y. Dede, F. Karadas, *Chem. A Eur. J.* **2018**, *24*, 10372–10382.
[43] G. Kresse, J. Furthmüller, *Phys. Rev. B: Condens. Matter Mater. Phys.* **1996**, *54*, 11169–11186.
[44] G. Kresse, J. Hafner, *Phys. Rev. B* **1994**, *49*, 14251–14269.
[45] G. Kresse, J. Hafner, *Phys. Rev. B* **1993**, *47*, 558–561.
[46] G. Kresse, J. Furthmüller, *Comput. Mater. Sci.* **1996**, *6*, 15–50.
[47] J. P. Perdew, K. Burke, M. Ernzerhof, *Phys. Rev. Lett.* **1996**, *77*, 3865–3868.

[48] P. E. Blöchl, *Phys. Rev. B* **1994**, *50*, 17953–17979.

[49] J. Paier, M. Marsman, K. Hummer, G. Kresse, I. C. Gerber, J. G. Angyán, *J. Chem. Phys.* **2006**, *124*, 154709.

[50] W. Kohn, A. D. Becke, R. G. Parr, *J. Phys. Chem.* **1996**, *100*, 12974–12980.

[51] A. D. Becke, *Phys. Rev. A* **1988**, *38*, 3098–3100.

[52] A. D. Becke, *J. Chem. Phys.* **1993**, *98*, 5648–5652.

[53] R. G. Parr, W. Yang, *Density-Functional Theory of Atoms and Molecules*, Oxford Univ. Press N. Y. **1989**.

[54] D. J. F. G. W. T. M. J. Frisch, H. B. Schlegel, G. E. Scuseria, M. A. Robb, J. R. Cheeseman, G. Scalmani, V. Barone, B. Mennucci, G. A. Petersson, H. Nakatsuji, M. Caricato, X. Li, H. P. Hratchian, A. F. Izmaylov, J. Bloino, G. Zheng, J. L. Sonnenberg, M. Hada, *Gaussian 09* **1988**, *37*, 785.

[55] C. Lee, W. Yang, R. G. Parr, *Phys. Rev. B* **1988**, *37*, 785–789.

[56] P. J. Hay, W. R. Wadt, *J. Chem. Phys.* **1985**, *82*, 270–283.

[57] P. J. Hay, T. H. Dunning, *Methods of Electronic Structure Theory*, Springer Boston MA, **1977**, 1–27.

[58] R. A. Kendall, T. H. Dunning, R. J. Harrison, *J. Chem. Phys.* **1992**, *96*, 6796–6806.

[59] T. Yanai, D. P. Tew, N. C. Handy, *Chem. Phys. Lett.* **2004**, *393*, 51–57.

[60] S. Miertus̃, J. Tomasi, *Chem. Phys.* **1982**, *65*, 239–245.

[61] S. Miertuš, E. Scrocco, J. Tomasi, *Chem. Phys.* **1981**, *55*, 117–129.

[62] J. L. Pascual-Ahuir, E. Silla, I. Tunon, *J. Comput. Chem.* **1994**, *15*, 1127–1138.

[63] Chemcraft - graphical software for visualization of quantum chemistry computations.https://www.chemcraftprog.com/.